Encoding Magnetic Anisotropies in Digital Light Processing 3D Printing

ADVANCED FUNCTIONAL MATERIALS
www.afm-journal.de

Encoding Magnetic Anisotropies in Digital Light Processing 3D Printing

*Eléonore Aïdonidis, Andrea Cosola, Pierre Bourdon, Hichem Dammak, Marco Sangermano, Frédéric Demoly, Marco Faustini, Amélie Pérot, Didier Lairez, Rakine Mouhoubi, Sébastien Blanquer, and Giancarlo Rizza**

Magnetic fields are increasingly used in 4D printing to program matter across multiple length scales, enabling control over both macroscopic structures and nanoscale particle organization. However, their integration into additive manufacturing remains limited by compatibility constraints—such as interference with extrusion or optical access—and the inherent challenge of generating spatially resolved, dynamic magnetic fields. In this work, a digital light processing 3D printing method is introduced that directly encodes programmable magnetic anisotropy during fabrication. By formulating a photocurable resin with magnetic nanoparticles and liquid crystal monomers, composite structures are fabricated that respond to both magnetic and thermal stimuli. A hybrid magnetic system—combining a nested Halbach array with a coaxial coil placed in its inner cavity—enables real-time, 3D control of magnetic fields (in both direction and intensity) during the printing process. This approach enables the alignment of liquid crystal mesogens, magnetic fillers, and the formation of vertically oriented nanoparticle chains. The resulting materials exhibit direction-dependent actuation, shape reconfiguration, and selective conductivity, demonstrating a versatile platform for creating multifunctional and multi-stimuli-responsive devices.

1. Introduction

The functional properties of a material refer to its capacity to interact with the surrounding environment and respond dynamically to external stimuli, such as temperature, light,[1] pH,[2] mechanical forces,[3] or even electric[4,5] and magnetic fields.[6] Integrating such materials into additive manufacturing—especially within the scope of 4D printing—opens the path to constructing structures capable of shape change or property modulation over time in response to specific triggers.[7–16] Among the various classes of smart materials for 3D printing, polymers are the most commonly employed. Their processability through extrusion-based (e.g., fused filament fabrication-FDM, direct ink writing-DIW) and vat photopolymerization (e.g., stereolithography-SLA, digital light processing-DLP, two-photon polymerization–2PP) methods

E. Aïdonidis, A. Cosola, P. Bourdon, D. Lairez, G. Rizza
Laboratoire des Solides Irradies (LSI)
CEA/DRF/IRAMIS
Ecole Polytechnique
Institut Polytechnique de Paris
Palaiseau 91128, France
E-mail: giancarlo.rizza@cea.fr

A. Cosola, M. Sangermano
Department of Applied Science and Technology
Politecnico di Torino
Corso Duca degli Abruzzi 24, Torino 10129, Italy

H. Dammak
Laboratoire Structures Propriétés et Modélisation des Solides (SPMS)
Université Paris-Saclay
CentraleSupélec, CNRS, Gif-sur-Yvette F 91190, France

F. Demoly
UTBM
CNRS
Université Marie et Louis Pasteur
ICB UMR 6303, Belfort 90010, France

F. Demoly
Laboratoire Interdisciplinaire Carnot de Bourgogne
CNRS
Université Bourgogne Europe
ICB UMR 6303, Dijon 21000, France

M. Faustini, A. Pérot
Chimie de la Matière Condensée de Paris
CNRS
Sorbonne Université
UMR 7574, Paris F-75005, France

F. Demoly, M. Faustini
Institut Universitaire de France
Paris 75231, France

R. Mouhoubi, S. Blanquer
CNRS
Université de Montpellier
Montpellier 27051, France

The ORCID identification number(s) for the author(s) of this article can be found under https://doi.org/10.1002/adfm.202523995

DOI: 10.1002/adfm.202523995

makes them suitable for fabricating complex architectures.[17–19] However, the performance of 4D-printed polymer structures is often constrained by limited mechanical strength or functional responsiveness.[20–24] A widely adopted strategy to overcome these limitations and improve the material's properties involves incorporating fillers—such as nanoparticles, fibers, or platelets—into the polymeric matrix to create nanocomposite systems.[25–28] The potential of these materials is further enhanced if embedded fillers can be manipulated to create well-ordered and/or anisotropic structures within the 3D-printed construct. In particular, this task can be accomplished by applying external forces or energies to drive the micro-to-nanoscale arrangement of nanomaterials within the printed structures.[29–44] Beyond the addition of fillers, however, an equally crucial strategy to improve the polymer's physicochemical, mechanical, and functional properties involves the structuring and anisotropic organization of the polymer matrix itself. In this context, external fields can also be employed to align mesophases, liquid crystal domains, or polymer chains within the host matrix.[45–47] Such control at the molecular or supramolecular level can impart directional mechanical and actuation properties to the 4D-printed object. In particular, magnetic fields show great potential in this dual role, as they can drive the self-assembly of magneto-responsive particles (e.g., Fe_3O_4 nanoparticles), as well as orient domains within a magneto-sensitive polymeric matrix, such as a liquid crystal elastomer (LCE).[48–50]

This enables the programming of bulk anisotropy and facilitates the fabrication of structures with spatially varying mechanical or actuation responses.

Liquid Crystal Elastomers (LCEs) are a pivotal class of smart polymers, valued because their precise, programmable shape changes depend entirely on controlling the internal mesogen alignment. Historically, conventional methods like mechanical, surface, and rheological alignment[51–54] struggle to impose this molecular order reliably within complex 3D printed architectures. The breakthrough lies in leveraging the material's magneto-responsiveness. LCE precursors possess an intrinsic diamagnetic susceptibility due to their aromatic structure, meaning their mesogens naturally align parallel to an applied magnetic field.[46] This magnetic field alignment is uniquely effective because it allows for the precise tuning of the molecular director throughout the material's bulk, without physically constraining the final part's geometry.[55] By integrating this magnetic control with vat photopolymerization (DLP), researchers can now create complex, highly functional magneto-responsive 3D structures. This synergy offers unprecedented spatial resolution and versatility, opening new frontiers for stimuli-responsive materials.[56–58]

On this basis, by combining field-assisted alignment of both the fillers and the matrix, one can adopt a multiscale design approach that bridges molecular orientation and macroscopic geometry. This unlocks new possibilities for the creation of highly heterogeneous, multifunctional devices—from soft robots to adaptive optics and tissue scaffolds—where local structure governs global function. Recently, a first attempt to encode both micro- and macro-structural anisotropies has been reported using extrusion-based DIW 3D printing of LCE matrices containing Fe_3O_4 nanoparticles.[59,60] However, the alignment relied on two distinct stimuli: shear forces during extrusion were used to orient the mesogens of the LCE matrix, while an external magnetic field directed the alignment of the magnetic fillers. In this work, we demonstrate that a single stimulus, such as—the applied magnetic field—can be used to program both micro- and macro-scale anisotropies by selectively tuning its parameters to control the orientation of either the matrix or the embedded fillers.

Recent advances in magnetically-driven 3D printing have introduced various methods for controlling magnetic fields during fabrication. These approaches fall into two main categories: systems using permanent magnets and those based on electromagnets—each offering trade-offs in cost, flexibility, and integration. The simplest setup uses a single permanent magnet, providing a compact and low-cost solution that can generate strong static fields (often >1 T). However, it only allows binary orientation (north/south) and suffers from nonuniform field distribution beyond the magnet's surface, where the field decays rapidly ($\propto r^{-3}$). This creates undesirable gradients, leading to uneven filler distribution and unpredictable forces in printed objects. Additionally, adjusting the field strength requires physically repositioning the magnet—a challenge in setups like DLP printers, where magnets can block light if placed above the vat. These limitations restrict permanent magnets mainly to configurations below the vat with top-down illumination.[61,62] To address spatial limitations, multi-magnet systems have been introduced. Configurations such as coaxial N–S magnet pairs, often coupled with motorized rotation stages, produce more uniform fields and allow directional control. The use of this approach has been recently reported for the magnetic alignment of LCE mesogens using DLP printers.[58] Electromagnets, by contrast, allow tunable field direction and strength via electric currents. Though typically limited to ≈20 mT due to power constraints, they are easy to integrate into 3D printers. Kim et al used a single-coil setup in DIW to reorient magnetic particles near the nozzle.[63] More advanced systems include Helmholtz coils, where two identical coils generate a uniform central field. Martin et al used a three-axis Helmholtz-DLP system for dynamic alignment of iron oxide-coated alumina microparticles[64] while Nakamoto et al employed five coils in SLA to align fibers vertically.[65] Emerging non-orthogonal electromagnet configurations offer more complex field geometries. Dai et al. demonstrated this in a robotic actuator with three magnetically controlled legs.[66] Finally, Halbach arrays have been recently used.[67] This principle traces back to John C. Mallison, who, in 1973, introduced the idea of single-sided flux for a planar magnetic arrangement with a constant-amplitude rotating vector magnetization.[68] This principle was later extended by Halbach to permanent multipole magnets by implementing the system for a loop configuration.[69]

Based on the insights from the preceding critical reviews that assessed the potential and limitations of current approaches to encoding magnetic anisotropies during 3D printing, we present a novel hybrid magnetic device designed to overcome key challenges, as illustrated in **Figure 1a–c**. This device combines the advantages of nested Halbach arrays and magnetic coils, enabling precise control over the homogeneity, spatial orientation, and intensity of the magnetic field, offering the unique opportunity to turn the field on and off at will at any time during the printing process.[70] It is robust, cost-effective, and fully compatible with vat photopolymerization-based additive manufacturing. Details of the experimental setup, numerical simulations, and integration of the device into a commercial DLP printer are provided in

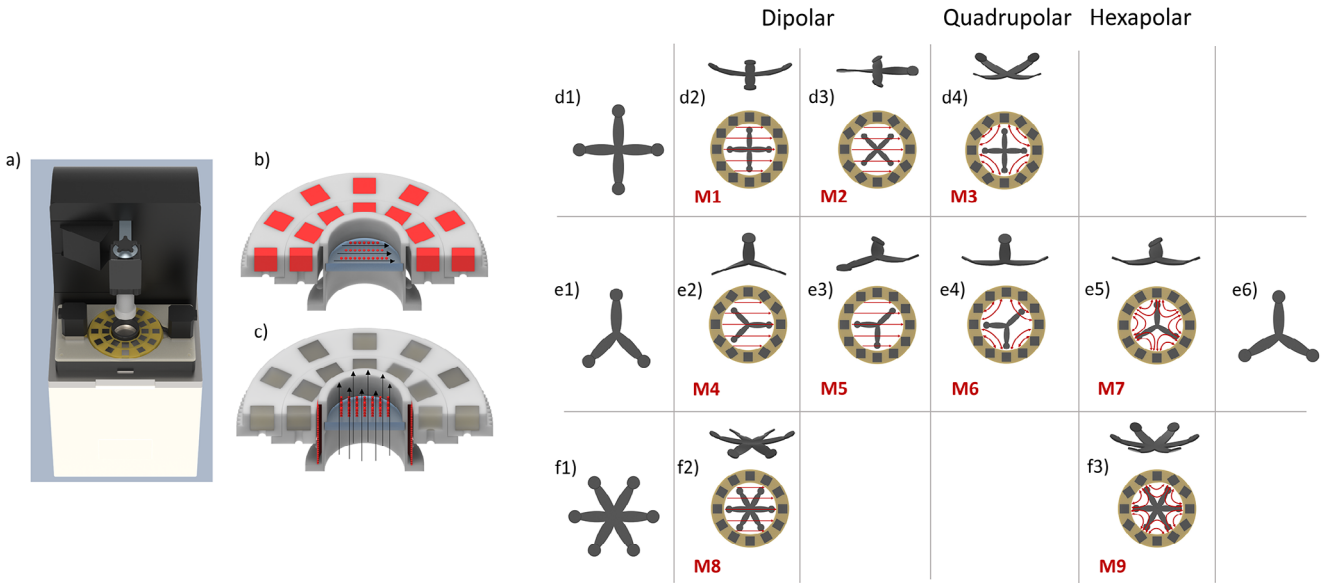

Figure 1. Hybrid magnetic device to fabricate programmable 4D-printed structures. a) schematic of the DLP printer integrating the device, allowing b) the magnetic field control in the horizontal plane using a nested Halbach array (in red), and c) in the vertical direction using a coaxial coil (in red) within the central region of the nested Halbach array. The direction of the field is indicated by the arrows. d–f) Designs of the printed structures, their relative orientation within the Halbach arrays, and the expected deformations. (d1-4) cross-shaped. (e1-4) Y-shaped tripod with arms positioned at 90° and 135°, and (e5-6) all three arms spaced at 120° angle. (f1-3) hexapod-shaped where all arms are spaced at 60°. M1 to M9 represent the activation modes resulting from the combination of printed structures (cross, Y-shaped tripod, and hexapod) with different Halbach array configurations (dipolar, quadrupolar, and hexapolar).

the Supporting Information. As a proof of concept, we demonstrate its use in fabricating programmable magneto-responsive structures, including multimodal actuators with multifunctional tunable directional response (**Figures** 1d,f, 2–5), and vertically stacked, electrically conductive nanostructures (**Figure** 6).

2. Results and Discussion

2.1. Strategy for Encoding Multimodal and Multifunctional Bending Actuations

Multimodal bending refers to the ability of a structure to undergo multiple, directionally distinct bending deformations in response to external stimuli. In printed structures, this control can be achieved by choosing specific Halbach array configurations, each of which generates a distinct magnetic field pattern that determines the resulting magnetic anisotropy. As described in Supporting Information, the Halbach cylinder can be segmented into P identical magnets having the same strength but a different planar orientation φ, set by the rule $\varphi = (k+1)\theta$, where θ is the magnet's position around the cylindrical array.[67,71,72] The value of the integer number k controls the magnetic field shape within the cylinder: $k = 1$ generates a uniform (dipolar) field, while $k = 2$ and $k = 3$ create more complex (quadrupolar and hexapolar) fields with increasing spatial gradients. Finally, the combination of two Halbach arrays in a nested coaxial configuration can be used to tune both the field intensity and direction in the x-y plane.

To exploit these tunable characteristics and highlight the system's multimodal capabilities (activation directions), four structures were designed (Figure 1). The first one is a symmetric cross, consisting of four segments (arms) of equal length (Figure 1d1), the second consists of a tripod arranged in a Y-shape, with two possible sub-configurations: either two arms positioned at a 90° angle, or all three arms spaced at 120°, as depicted in Figure 1e1,e6. The last one is a hexapod with six arms evenly spaced at 60° in a radial pattern (Figure 1f1). Figure 1d2–f3 illustrate how the encoding of distinct deformation modes is enabled by the orientation of these structures relative to the magnetic field lines produced by Halbach arrays. For instance, three activation modes (M1, M2, and M3) would be encoded by the cross structure. Modes M1 and M2 utilize a dipolar Halbach configuration: in M1, the magnetic field lines align with the long axis of two arms and the short axis of the other two (Figure 1d2; Movie S10, Supporting Information); in M2, the cross is rotated so that all four arms are positioned at 45° to the field lines (Figure 1d3). Mode M3 employs a quadripolar Halbach configuration, aligning the magnetic field along the long axis of all four arms (Figure 1d4; Movie S12, Supporting Information). The Y-shaped structure has a configuration that permits greater flexibility and demonstrates four activation modes (M4, M5, M6, and M7). M4 mode uses a dipolar Halbach setup to align a single arm with the field while the other two sit at 45° (Figure 1e2). By rotating the structure by 45°, mode M5 allows for three different alignments, where one arm is parallel (0°), one normal (90°), and one at 45° to the applied field (Figure 1e3). M6 is based on a quadripolar Halbach configuration where two arms are aligned with the field and the third one is unaligned (Figure 1e4). Finally, for mode M7, all three arms are spaced at 120°, and a hexapolar Halbach configuration is used such that all the arms are aligned along the field (Figure 1e5). The hexapod structure supports two activation modes (M8 and M9). In M8, a dipolar Halbach configuration aligns two arms with the field and the remaining four

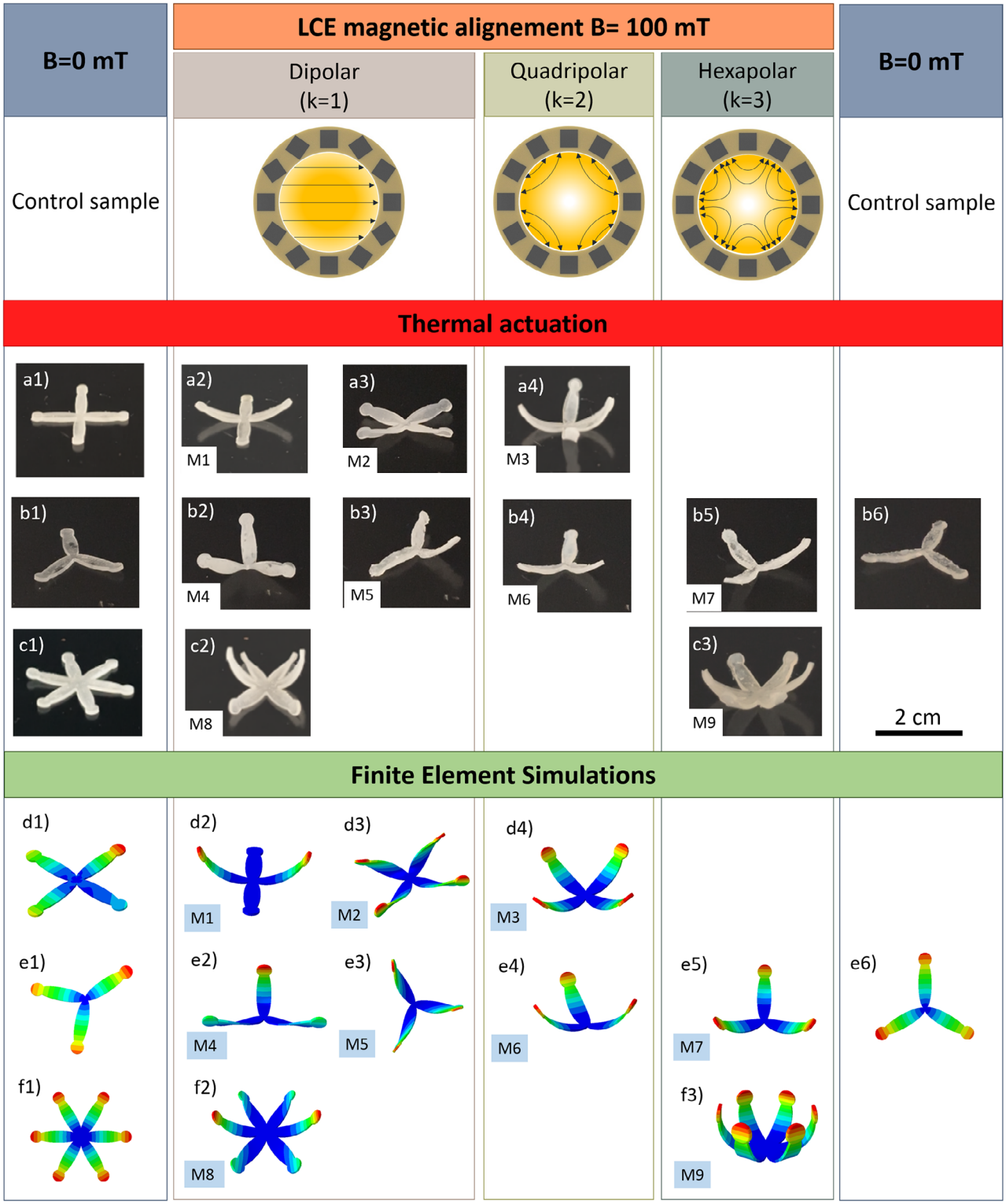

Figure 2. Multimodal thermal actuation of LC resins printed in the nematic phase. (a1), (b1), (c1), and (b6) represent the control samples that are printed without applying a magnetic field (B = 0 mT). Actuation modes (M1–M9) of various printed LCE structures under different Halbach magnetic field configurations. For the cross-shaped structure, (a2) dipolar fields activate two arms (M1), while (a3) a 45° rotation results in twisting of all four arms (M2); (a4) quadrupolar fields induce bending in all arms. In Y-shaped structures, (b2) dipolar configurations yield mixed actuation: two twisted and one bent arm (M4), and (b3) one twisted, one bent, and one inactive arm (M5). (b4) Quadrupolar fields cause two arms to bend (M6), and (b5) hexapolar fields actuate all arms (M7). For the hexapod structure, (c2) dipolar fields bend only two arms while twisting the other four (M8), while (c3) hexapolar fields activate all six (M9). d-f) finite element simulations of thermo-responsive LCE, see Figure S13, Supporting Information.

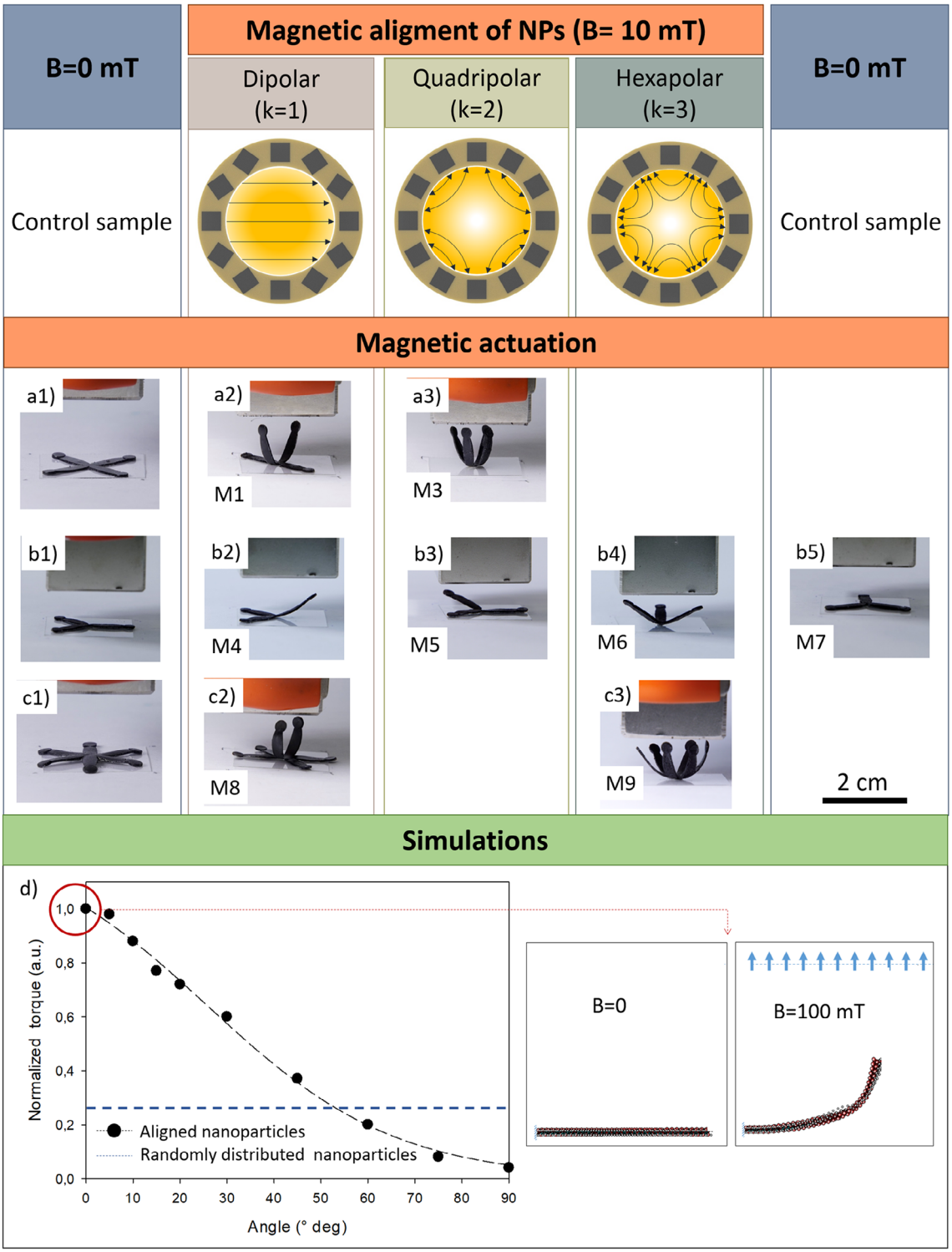

Figure 3. Multimodal magnetic actuation of composite LCEs embedding Fe_3O_4 nanoparticles and printed in isotropic phase. (a1), (b1), and (c1) show control samples printed without applying a magnetic field (B = 0 mT), resulting in isotropic dispersion of Fe_3O_4 nanoparticles. For the cross-shaped structure, a2) corresponds to actuation mode M1, where two arms are activated, while a3) shows mode M3, in which all four arms are simultaneously engaged. In Y-shaped structures, (b2) shows mode M4 with a single activated arm, (b3) corresponds to mode M6 with two activated arms, and (b4) displays mode M7 with full three-arm actuation. For the hexapod structure, (c2) illustrates mode M8, where actuation occurs in two arms aligned with the field, while (c3) shows mode M9, in which a hexapolar Halbach configuration enables coordinated activation of all six arms. (d) Molecular dynamics simulation showing how the bending torque magnitude varies with the angle between the nanoparticle chains and the printed arm's long axis, normalized with respect to the torque at zero angle, Movie S13 (Supporting Information). The dashed line corresponds to the value for randomly distributed nanoparticles, see Figure S14, Supporting Information.

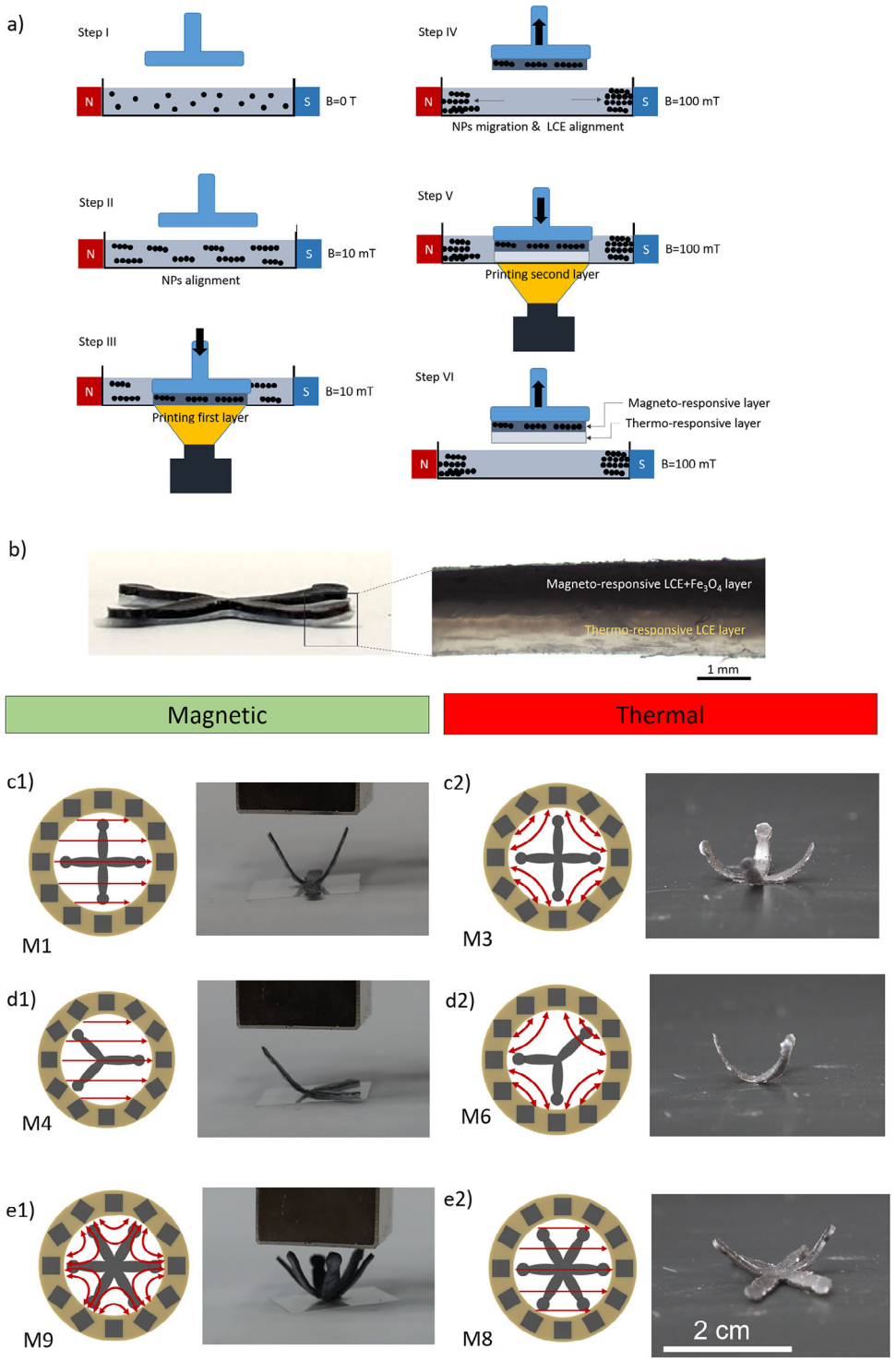

Figure 4. Multimodal thermo-magnetic actuation in composite LCEs embedding Fe_3O_4 nanoparticles. a) Schematic of the fabrication sequence for a thermo-magnetic bifunctional material. b) Cross-sectional optical image showing a bilayer structure composed of isotropic Fe_3O_4 nanoparticle chains within non-aligned LCE mesogens (dark color) and an aligned LCE layer (bright color). Distinct magnetic modes were encoded in three architectures: cross-shaped, Y-shaped, and hexapod. For the cross, (c1) shows magnetic mode M1 with two activated arms, while (c2) shows thermal mode M4 engaging all four arms. In the Y-structure, (d1) corresponds to magnetic mode M4 with one activated arm, and (d2) to thermal mode M6 activating all arms. For the hexapod, (e1) represents magnetic mode M9, where a hexapolar Halbach configuration drives coordinated activation of six arms, and (e2) thermal mode M8, inducing two bending and four twisting deformations.

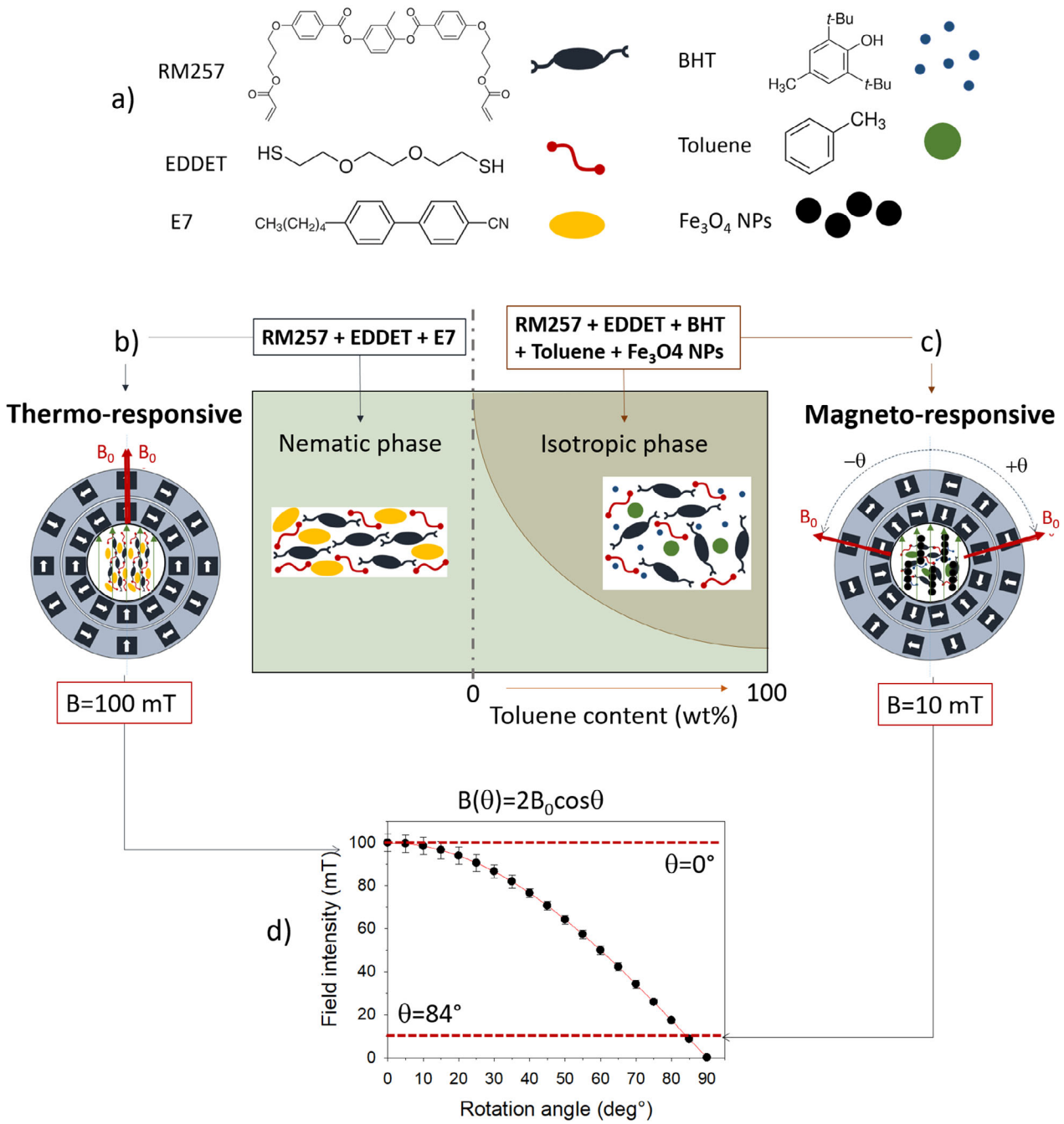

Figure 5. Chemicals involved in the resins synthesis (a) and phase diagram of liquid crystal organization showing the two photocurable resins used to create b) thermally (RM257+EDDET+E7+BAPO) and c) magnetically (RM257+EDDET+BHT+Toluene+BAPO) responsive 3D-printed features. d) Nested Halbach cylinder configuration with co-aligned magnetic fields, generating a field intensity of 100 mT, used for fabricating thermo-responsive features. $B_0 = 50$ mT represents the maximum magnetic field generated by each Halbach array. The nested configuration, in which the arrays are rotated by $\pm\theta$ respectively, produces a total field $B = 2B_0 \cos\theta$. d) Nested configuration with two co-aligned Halbach arrays (θ =0°) generates a field intensity of 100 mT, while when they are rotated by 84° in clockwise and anticlockwise directions, a field intensity of 10 mT is produced. The former configuration is used to a produce thermo-magnetic element, whereas the latter for fabricating magneto-responsive features.

at 60° (Figure 1f2, Movie S11, Supporting Information), whereas M9 uses a hexapolar Halbach configuration to align all six arms with the magnetic field (Figure 1f3).

After establishing the strategy to introduce directional magnetic anisotropies, the next objective is to demonstrate multi-functionality. Specifically, this involves showing that directional (multimodal) deformations can be triggered by various stimuli. This is done by using photocurable LCs. Notably, LCEs exhibit distinct phases based on the ordering of their mesogens.[46,73] In the nematic phase, the mesogens align to produce long-range

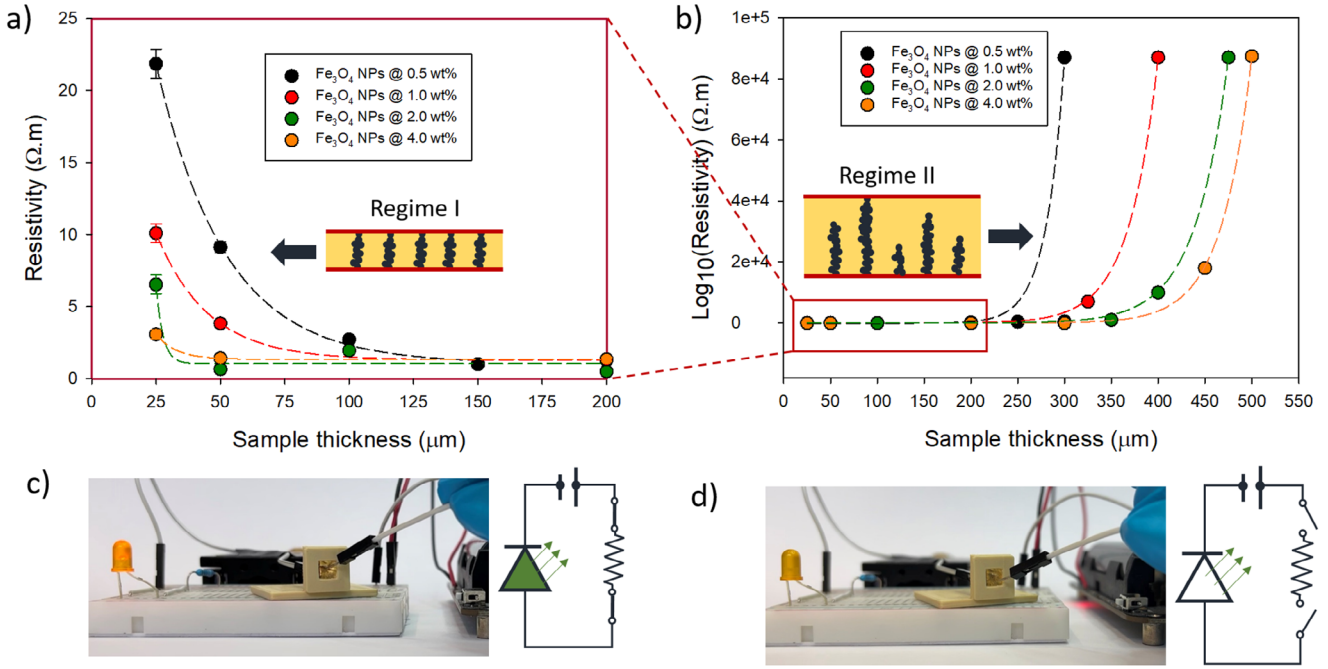

Figure 6. Resistivity measurements as a function of sample thickness reveal two regimes: a) Regime I (≤ 200 μm) shows an exponential decrease in resistivity with increasing thickness and Fe_3O_4 content, reflecting improved charge transport; b) Regime II (> 200 μm) exhibits an exponential increase in resistivity up to 10^5 Ω·m, indicating a transition to insulating behavior. Samples used as resistive component of an electric circuit: c) In Regime I, the LED lights up under an applied voltage of 5 volts, (d) whereas in Regime II, the sample's resistivity is too high to allow LED activation.

orientational order and anisotropic properties, which is defined as a nematic monodomain state; whereas in the isotropic phase, the mesogens are randomly oriented, resulting in isotropic behavior of the material. LCEs actuate by undergoing a reversible shape change when their mesogens transition from an ordered nematic phase to a disordered isotropic phase, causing the polymer network to deform. Multifunctionality can be achieved by appropriately tuning the formulation (Figure 5a) so that the LC resin can be printed in either the nematic or the isotropic phase. When printed in the nematic phase (Figure 5b), actuation is driven by thermal stimuli that induce nematic-to-isotropic phase transitions. Conversely, when printed in the isotropic phase in the presence of toluene, the mesogens are not aligned in a monodomain state and thermal actuation is not possible (Figure 5c). In this case, the LC resin serves simply as a soft, inert matrix for dispersing nanofillers. If these nanofillers are magnetic nanoparticles, the resulting elastomeric material becomes magnetically active. Finally, the application of a specific magnetic field is required to achieve either thermal or magnetic responsiveness in a multimodal construct, which can be generated by appropriately rotating two nested Halbach arrays (Figure 5d).

2.2. Multimodal Thermo-Responsive LCE Actuations

To fabricate the nematic LCE networks, we employed a photopolymerization process based on acrylate–thiol chain transfer[74] (Figure 5b). The mesogenic diacrylate RM257 (1,4-Bis[4-(3-acryloyloxypropyloxy)benzoyloxy]-2-methylbenzene) was used as the primary monomer, and EDDET (2,2′-(ethylenedioxy)diethanethiol) served as the dithiol chain extender. Since RM257 alone does not exhibit a nematic phase below its melting point ($T_m \approx 69$ °C), we added a nonreactive mesogenic solvent E7 (4-cyano-4′-pentylbiphenyl) at a 1:1.5 weight ratio to obtain a stable nematic phase at room temperature. The presence of this nematic phase at room temperature is essential for aligning the mesogens under an external magnetic field during printing—an effect supported by previous work,[46] and experimentally confirmed by polarized optical microscopy (POM) and wide-angle X-ray scattering (WAXS), as shown in Figures S10 and S20 (Supporting Information). Moreover, differential scanning calorimetry (DSC) analysis showed a decrease in the nematic–isotropic transition temperature of the mixture to $T_{ni} = 68.8$ °C, compared to $T_{ni} \approx 126$ °C for pure RM257 (Figure S9, Supporting Information).

Recent studies have shown that a field strength of ≈ 100 mT is necessary to achieve effective nematic alignment.[56,75] However, as the magnetic field strength decreases with distance ($B \sim r^{-3}$), where r is the inner radius of the Halbach array, achieving high field intensities with a Halbach array requires reducing its inner diameter, which in turn limits the printable surface area. To address this point, concentric Halbach arrays in nested configuration were designed and, for the first time, implemented in a DLP printer (Section S.1, Supporting Information). This design enhances the magnetic field by leveraging the principle of vectorial superposition. This approach enables reaching the required 100 mT field strength while maintaining an acceptable printing surface of $\approx A = \pi d^2/4 \sim 12$ cm^2, where $d = 4$ cm is the inner diameter for the used Halbach array. Finally, the

build platform of the DLP printer (Asiga Max X27, Sydney, Australia) was also modified to make it compatible with the Halbach array configuration (Figure 1a,b). Activating the magnetic field while the LC resin is still in its liquid state allows the photopolymerization process to fix the mesogens in a specific magnetic alignment. This results in a 3D-printed structure whose internal orientation follows the applied field pattern, as shown in Figure 1.

First, we show that the samples printed without applying the magnetic field (Figure 2a1,b1,c1,b6; Movies S1 and S2, Supporting Information) do not undergo deformation when placed on a heated plate above 120 °C, confirming that magnetic alignment is necessary to activate the actuation of the samples. Each arm of the printed LCE features can be viewed as a cantilever—fixed at one end and free at the other—allowing their thermally induced actuation to be directly connected to the mesogen orientation. This orientation is, in turn, determined by the alignment of the structure relative to the magnetic field generated by the Halbach arrays, as illustrated in Figure 1. When mesogens are aligned along the arm's length of the structure, a bending toward the vertical direction is observed. If the mesogens are oriented along the short axis, contraction occurs across the width, resulting in minimal deformation, whereas when the mesogens are angled at 45°, heating induces a torsional response, causing the free end of the beam to twist out of the plane. It is worth noticing that, depending on the polarity k of the used Halbach array as well as the shape of the structure that was designed, multimodal deformations are possible within a printed structure. The actuation of the different modes (M1–M9) is shown in Figure 2. For the sake of example, for the cross structure, in mode M1, only two arms bend if a dipolar Halbach configuration is used (Figure 2a2, Movie S3, Supporting Information). However, if the cross is rotated by 45°, mode M2, the same structure shows the twist of all four arms (Figure 2a3; Movie S5, Supporting Information), while in the quadrupolar Halbach configuration (mode M3), all four arms exhibit bending (Figure 2a4; Movie S4, Supporting Information). For the Y-shaped structures in dipolar Halbach configuration, mode M4 features two twisted arms and one bent arm (Figure 2b2; Movie S6, Supporting Information), while mode M5 exhibits one twisted arm, one bent arm, and one inactive arm (Figure 2b3). In the quadrupole Halbach configuration, mode M6 shows two bent and one inactive arm (Figure 2b4), and in the hexapolar Halbach configuration, mode M7 exhibits all arms bending (Figure 2b5). Finally, for the hexapod structure in dipolar Halbach configuration, only two arms are active (bending) (Figure 2c2; Movie S7, Supporting Information), which increases to six when the hexapolar Halbach configuration is used (Figure 2c3). Finite element (FE) simulations of the thermoresponsive LCE behavior are shown in Figure 2d–f) and described in S.13 (Supporting Information). These FE simulations provide highly accurate predictions of the complex shape changes upon thermal actuation. The good agreement between the predicted deformations and the experimentally printed structures validates the model's ability to capture the underlying physics of encoded mesogen alignment.

2.3. Multimodal Magneto-Responsive LCE Nanocomposite Actuations

As a second demonstration of the device's multimodal activation capability, we highlight its use in printing magnetoresponsive composites. In this case, the main challenge lies in introducing magnetic anisotropy by aligning Fe_3O_4 nanoparticles without relying on the mesogen alignment. This approach ensures that actuation is driven purely by magnetic interactions, while the LCE matrix contributes solely through its elastomeric properties. To achieve this, the photocurable LC resin was specifically optimized to remain in the isotropic phase at room temperature throughout the printing process (Figure 5c). A mesogenic diacrylate RM257 was used as the primary monomer, and EDDET as the dithiol chain extender, while BHT (2,6-di-tert-butyl-4-methylphenol, 0.5 wt.%) was added as a free-radical inhibitor to improve the storage stability of the resin, and BAPO was used as the photoinitiator for subsequent light-induced polymerization. Finally, toluene was incorporated into the formulation at increasing concentrations. DSC revealed a progressive suppression of the nematic phase with higher toluene content (Figure S8, Supporting Information), such that above 50 wt.% toluene, the nematic phase disappeared, and the formulation displayed an isotropic phase at room temperature, as confirmed by polarized optical microscopy (POM) and wide-angle X-ray scattering (WAXS) (Figures S10 and S20, Supporting Information). Magneto-active elastomers were obtained by embedding commercially available 100 nm soft magnetic nanoparticles (Fe_3O_4) at 4 wt.% into the LC formulation. As previously reported,[14] a magnetic field of ≈ 10 mT is sufficient to induce the self-assembly of nanoparticles into chains oriented along the field direction. This can be achieved by appropriately rotating the two nested cylindrical Halbach cylinders by an angle of $\theta = 84°$ in clockwise and counterclockwise directions via remote control, using an Arduino microcontroller (Figure 5d). Under the influence of an external magnetic field, Fe_3O_4 nanoparticles align into linear chains along the field direction through dipole–dipole interactions.[76] Owing to their elongated shape, these chains display magnetic anisotropy, with a well-defined easy axis of magnetization, thereby imparting anisotropic magneto-mechanical properties to the embedding matrix.[77] In contrast to the thermally driven LCEs, magneto-active LCEs nanocomposites can be actuated by magnetic torque ($\tau = m \times B$), where m is the magnetic moment vector, allowing the sample's arm to align along the applied field. Thus, only the bending effect can be experimentally observed. The actuation of the different modes (M1-M9) is shown in Figure 3, and corresponding movies are available in the Supporting Information. First, we demonstrate that printed samples containing dispersed Fe_3O_4 nanoparticles—i.e., without chain formation during the printing step (B = 0 mT)—do not exhibit any deformation when exposed to an external magnetic field. Indeed, as shown in Figure 3a1, b1, b5, c1; Movies S8 and S9 (Supporting Information), no actuation occurs for any of the designed shapes when placed above a 3 × 3 × 3 cm^3 cubic permanent magnet generating a 90 mT field, perpendicular to the plane of the objects. As previously reported,[77] this confirms that

magnetic alignment of the nanoparticles during printing is essential to induce torque actuation under an external magnetic field. Second, we show the different actuation modes when samples are printed under a magnetic field. In the case of the cross-shaped structures, two distinct actuation modes are observed: mode M1 involves the activation of two arms (Figure 3a2; Movie S10, Supporting Information), while mode M3 engages all four arms simultaneously (Figure 3a3; Movie S11, Supporting Information). For the Y-shaped structures, the number of activated arms varies with the configuration: one arm in mode M4 (Figure 3b2), two arms in mode M6 (Figure 3b3), and all three arms in mode M7 (Figure 3b4). Finally, the hexapod structure exhibits mode M8 when the magnetic field aligns with the long axis of two arms and the short axis of the other two (Figure 3c2). In mode M9, a hexapolar Halbach configuration is used to align the magnetic field along the long axis of all six arms (Figure 3c3; Movie S12, Supporting Information), enabling coordinated multi-arm actuation.

To understand why no bending is observed when the nanoparticle chains are oriented at an angle $\theta = 60°$ or 90° relative to the arm's main axis, we developed a simple model (described in the Supporting Information). This model estimates the magnetic torque exerted by a magnet placed at a distance equal to the magneto-responsive arm's length, with the arm fixed at one end. The applied magnetic field, ≈ 100 mT, far exceeds the material's coercive field (≈ 13 mT).[16] Under these conditions, the remanent magnetic moments of the nanoparticles—initially aligned along the printing field—can reorient collectively along the local field imposed by the external magnet and nearby particles. Thus, each nanoparticle experiences an attractive force due to the magnetic field, and the cumulative effect of these forces generates a macroscopic torque that tends to rotate the chains. The system thus behaves like an elongated ellipsoidal cluster of paramagnetic nanoparticles, with anisotropic magnetic susceptibility and an easy magnetization axis along the chain direction.[78] This mechanism explains why arms containing chains aligned parallel to their main axis respond strongly and consistently to the external magnetic field, bending toward the magnet regardless of the printing field direction. In contrast, Figure 3d shows that the bending torque decreases by 60% when the angle θ increases from 0° to 45°. This reduction is even more pronounced at 60° and 90°, reaching 80% and 96% respectively, resulting in a torque lower than that estimated for randomly distributed nanoparticles in the arm.

2.4. Multimodal and Multifunctional Thermo-Magneto-Responsive LCE Nanocomposite Actuations

In Sections 2.2 and 2.3, we demonstrated the device's ability to magnetically align components requiring different field strengths (≈ 100 mT for LCEs and ≈ 10 mT for magnetic NPs). Accordingly, we fabricated objects that were exclusively thermo-active (monodomain nematic LCEs, Section 2.2) or magneto-active (polydomain nematic LCE and Fe_3O_4 NPs, Section 2.3). Here, we address the challenge of printing an object that integrates both thermal and magnetic activation mechanisms, thereby demonstrating true multifunctionality through the simultaneous coupling of both alignment processes. This was achieved using the formulation described in Section 2.2 (RM257 + EDDET + E7, in the monodomain nematic phase), into which Fe_3O_4 NPs were incorporated at 4 wt.%. To decouple the thermal and magnetic effects, Fe_3O_4 nanoparticles were deliberately left non-functionalized, thereby preventing grafting onto the LCE mesogens and avoiding potential cross-interactions.

The strategy we adopted to introduce the multifunctionality is based on the following experimental observations. Fe_3O_4 nanoparticles remain homogeneously dispersed within the resin up to an applied magnetic field of ≈ 10 mT.[46] At higher field strengths, the fillers migrate along the direction of the applied field, leading to a depletion of the printing zone. In contrast, the alignment of mesogens requires magnetic fields exceeding ≈ 100 mT. As a result, it is not possible to simultaneously achieve both nanoparticle and mesogen alignment within a single printed layer. To overcome this limitation, we exploited controlled nanofillers migration to fabricate a bilayer element composed of two superposed layers that respond differently to stimulation through magnetic and thermal, Figure 4a. Specifically, the first layer is printed under a magnetic field of 10 mT for 2 min, enabling the formation of homogeneously distributed chains of magnetic fillers while the LCE mesogens remain unaligned, Steps I-II. Photocuring under these conditions fixes the material into a magnetically aligned configuration determined by the employed Halbach array (dipolar, quadrupolar, or hexapolar), Step III. The magnetic field is then increased to 100 mT for 10 min to align the mesogens while promoting the migration of nanoparticles out of the printing region, step IV. A second photocuring step stabilizes this configuration, producing a pattern determined by the chosen Halbach array, Step V. This approach enables the fabrication of multifunctional bilayer architectures, Step VI and Figure 4b.

Multimodality is achieved by printing the same geometries for both layers—such as cross-shaped, Y-shaped, or hexapod architectures—while encoding distinct magnetic field patterns (dipolar, quadrupolar, or hexapolar) for each layer. This design approach adds an extra level of tunability, endowing the printed constructs with programmable **multifunctionality** and **multimodality**, Figure 4c-e. These capabilities are illustrated through a series of distinct yet interconnected thermo-magnetic actuation modes (M1–M3, M4–M6, and M8–M9) obtained on the same element. For the cross-shaped structure, the magnetic mode M1 is programmed with a dipolar Halbach array, which selectively bends two opposite arms (Figure 4c1; Movie S14, Supporting Information). The thermal mode M3, obtained using a quadrupolar array, instead causes all four arms to bend simultaneously (Figure 4c2; Movie S15, Supporting Information). In the Y-shaped tripod, the magnetic mode M4 (dipolar array) activates only one arm (Figure 4d1; Movie S16, Supporting Information), while the thermal mode M6 (quadrupolar array) produces bending in all arms (Figure 4d2; Movie S17, Supporting Information). For the hexapod, the magnetic mode M8 (hexapolar array) activates all the arms (Figure 4e1; Movie S18, Supporting Information), whereas the thermal mode M9 (dipolar configuration) generates a combined deformation, with two arms bending and four twisting (Figure 4e2).

2.5. Charge Transport in Vertically Aligned Fe_3O_4 Nanoparticle Networks

To ensure compatibility with VAT-based photopolymerization, the Halbach cylinders are designed to generate magnetic fields parallel to the build platform, i.e., in the *x*-*y* plane. However, as mentioned in the introduction, our device also enables precise control of the magnetic field along the vertical (*z*) axis. This three-dimensional field-tuning capability is achieved by integrating a coaxial coil within the central region of the nested Halbach cylinder (see Supporting Information). The coil generates a magnetic field along the *z*-direction, described by $B_z = \mu_0 NI$, where μ_0 is the *vacuum* permeability, N is the number of turns per unit length, and I is the current through the coil. This configuration allows the generation of vertical magnetic fields up to 10 mT (Figure S5, Supporting Information), thereby expanding the range of programmable field orientations during printing and offering greater flexibility for magnetic alignment of nanoparticles within the resin. To demonstrate its capabilities, the device was used to fabricate vertically conductive pathways within the printed structures. To facilitate electrical measurements and microscopy preparation, a stiffer photocurable resin—bisphenol A ethoxylate diacrylate (BEDA)- was employed. Magnetic nanocomposites with integrated electrical functionality were then printed from a formulation comprising BEDA, Fe_3O_4 nanoparticles, and BAPO as photoinitiator. Single layers with thicknesses ranging from 25 to 500 µm and Fe_3O_4 concentrations between 0.25 and 4.0 wt.% were printed using material test parameters (Figure S12, Supporting Information). To induce vertical alignment of the nanoparticles, a 10 mT magnetic field was applied to the liquid resin for 30 s prior to printing. After fabrication, a 100 nm gold layer was deposited on both surfaces of each sample to enable resistivity and current–voltage (I–V) measurements (Figures S16 and S17, Supporting Information).

Resistivity measurements, presented in **Figure 6**, reveal two distinct regimes. The first, Regime I, is observed for sample thicknesses up to ≈ 200 µm and is characterized by an exponential decrease in resistivity with increasing thickness, as shown in Figure 6a,c. Concurrently, resistivity is also found to decrease with increasing Fe_3O_4 nanoparticle content in the resin. In Regime II (Figure 6b,d), corresponding to sample thicknesses above ≈ 200 µm, the trend reverses: resistivity increases exponentially with thickness, rapidly reaching values on the order of 10^5 Ω·m. This sharp rise indicates a transition to insulating behavior, likely to reduce percolation of conductive paths over larger distances.

To describe the resistive behavior of the printed layers, we developed a statistical model assuming chain lengths of vertically aligned magnetic nanoparticles follow a Gaussian distribution with mean length L_m and standard deviation σ (Figure S13, Supporting Information). We assume that only chains longer than the film thickness d can span the entire layer and contribute to electrical conduction. Each conductive chain behaves as a resistor with resistance R_0, and the chains are uniformly distributed with a surface density η (directly related to the initial nanoparticle concentration). Under these assumptions, the film's resistivity can be expressed as (Figure S10, Supporting Information):

$$\rho(d) = \frac{2R_0}{\eta d} \frac{1}{Erfc\left(\frac{d-L_m}{\sqrt{2}\sigma}\right)} \quad (1)$$

where Erfc is the complementary error function.

From the analysis of Equation (1), two experimentally observed regimes can be identified: For $L_m > d$, most of the chains are long enough to bridge the film. In this case, the argument of the error function becomes a constant, i.e., the Erfc ≈ constant, and the resistivity simplifies to:

$$\rho(d) \propto \frac{1}{\eta d} \quad (2)$$

Thus, in regime I, resistivity exhibits a clear inverse relationship with film thickness: $\rho(d) \propto 1/d$. However, the surface concentration η also plays a critical role. At small thicknesses, lower concentrations of contacted chains lead to higher resistivity due to fewer conductive chains per unit area. As the film thickness increases, these differences gradually diminish, as the geometric factor (i.e., the $1/d$ scaling) becomes dominant, causing resistivity values to converge. For $L_m < d$, only a small fraction of chains is long enough to span the film thickness. As d increases, the argument of Erfc grows rapidly, leading to a sharp rise in resistivity, primarily driven by the exponential decrease in the number of bridging chains. In this regime, $\rho(d)$ exhibits strongly nonlinear behavior.

Next, we further evaluate how nanoparticle dispersion and concentration influence the electrical behavior of the composites by analyzing their current–voltage (I–V) characteristics over a –5 V to +5 V range. The resulting I–V curves (Figure S17, Supporting Information) exhibit linear conduction at low voltages, indicative of Ohmic behavior, and suggesting that charge transport is dominated by direct conduction pathways formed by well-connected nanoparticle chains.

Finally, we evaluate whether electrical conductivity could be preserved when multiple layers were printed sequentially (Figure S18, Supporting Information). The goal was to assess the feasibility of vertical integration and interlayer electrical connectivity within the stacked structure. However, the results were negative, as no measurable conductivity was observed between layers. This is likely due to the low probability that nanoparticle chains from adjacent layers align perfectly to form continuous conductive paths across the interfaces. In the Supporting Information, we estimated the probability of interlayer connectivity as a function of filler concentration. It provides a useful estimate for the probability of electrical contact and highlights a key parameter for optimization. In particular, it suggests that adjusting the concentration of embedded nanostructures—provided that good printability is maintained—could enable reliable electrical contact in multilayer printed architectures. If successful, the approach will offer a robust platform for directional charge transport and integration into three-dimensional device architectures.

3. Conclusion

In this work, we present a scalable and versatile approach to encode magnetic anisotropy directly during DLP 3D printing,

enabling the creation of 4D-printed composites with tailored, multifunctional properties. To overcome the geometric and optical constraints typically associated with anisotropy induction in photopolymerization-based printing, we developed a hybrid magnetic setup that combines nested Halbach arrays with a central coil. This configuration offers precise, real-time control of fully tunable 3D magnetic fields—including their spatial direction, gradient, and intensity—while preserving transparency of the printing vat. This enables controlled spatial alignment of anisotropic fillers during crosslinking, unlocking new possibilities for spatially programming functional responses.

Besides, this platform enables the fabrication of multifunctional architectures exhibiting complex, direction-dependent actuation modes arising from the synergistic coupling of aligned mesogens and magnetically ordered nanoparticle chains. Such dual-responsive structures can undergo either independent magnetic or thermal actuation, or a combined multimodal response within a single printed element, while programmable field configurations—dipolar, quadrupolar, or hexapolar—allow selective activation of deformation pathways in Y-junction, cross, and hexapod geometries. Finally, we also achieve vertical alignment of Fe_3O_4 nanoparticle chains, producing embedded, electrically conductive nanostructures within printed components. This dual mechanical–electronic functionality paves the way for advanced applications in soft robotics, reconfigurable electronics, and multifunctional sensing. Altogether, this platform establishes a new direction in magnetically assisted 3D printing, where fine-tuned magnetic control, multimaterial responsiveness, and integrated microstructural design converge in a single fabrication step—laying the foundation for next-generation intelligent soft systems.

4. Experimental Section

Materials: 1, 4-Bis[4-(3-acryloyloxypropyloxy)benzoyloxy]-2-methylbenzene (≥95%, RM257) was purchased from Smolecule (San Antonio, USA). 2, 2-(Ethylenedioxy)diethanethiol (≥95%, EDDET), Toluene (≥99, 5%), 2, 6-di-tert-butyl-4-methylphenol (≥99%, BHT), phenylbis(2,4, 6- trimethylbenzoyl)phosphine oxide (≥97%, BAPO), Iron(II, III) oxide (50–100 nm, 97% purity, magnetite), and Bisphenol A ethoxylate diacrylate (BEDA) were purchased from Sigma–Aldrich (France). 4-Cyano-4′-pentylbiphenyl (≥98%, E7) was purchased from TCI (via https://zentek.it/). All chemicals were used as-received without further purification.

Preparation of the Isotropic Formulation: In an amber flask, RM257, BHT (0.5 wt.%), and BAPO (2 wt.%) were introduced, followed by the addition of toluene at a weight ratio of 1:1 (with respect to RM257). Toluene was used to stabilize the isotropic phase at room temperature. BHT was included as a free-radical inhibitor to enhance the storage stability of the resin. BAPO acted as a photoinitiator for subsequent UV-induced polymerization. The mixture was heated to 80 °C for 5 min to reach the isotropic state. After cooling to room temperature, EDDET was added at an acrylate-to-thiol molar ratio of 1.2:1, and the resulting isotropic mixture was homogenized using vortex mixing. Finally, magnetite (4 wt.%) was incorporated and dispersed using an ultrasonic bath.

Preparation of the Nematic Formulation: RM257 and the nematic liquid crystal E7 were combined in an amber flask at a weight ratio of 1:1.5. BAPO (2 wt.%) was then added. The mixture was heated to 90 °C for 5 min and subsequently cooled to room temperature, at which point the mixture remained in the nematic phase due to the stabilizing effect of E7. EDDET was added dropwise (acrylate-to-thiol molar ratio of 1:1), and the formulation was homogenized by vortex mixing.

Preparation of the Magneto-Electrical Formulation for Charge Transfer Experiments: Bisphenol A ethoxylate diacrylate (BEDA) was combined with a photoinitiator solution prepared by dissolving BAPO (2 wt.%) in acetone (10 wt.%) at 40 °C under gentle stirring. The resulting mixture was homogenized using a mechanical stirrer at 500 rpm. Magnetite nanoparticles were then incorporated into the resin at various weight concentrations ranging from 0.5 to 4 wt.% and vortexed prior to use to ensure uniform dispersion of the magnetic filler.

Material Test Calibration Procedure: Preliminary exposure tests were performed to calibrate the light-curing parameters for each formulated resin (see S.5, Supporting Information). Using the Spot Timer function of the Asiga 3D printer, a circular spot of 1.5 mm diameter was projected onto a resin layer in the resin tank. Exposure times ranged systematically from 0.1 to 15 s, depending on the resin's reactivity. After each exposure, the cured sample was removed and its thickness measured. Plotting the cured thickness against exposure time showed a logarithmic trend, from which an empirical equation was established. This equation was used to determine the exposure times needed to obtain the desired layer thicknesses during printing.

DLP Printing: All geometries were designed using Fusion 360 and exported as STL files. Three-dimensional structures were fabricated using a DLP printer (ASIGA Max X27) equipped with a 385 nm UV light source operating at an intensity of 59 mW cm^{-2}. The printing parameters were optimized for each formulation using the material test calibration procedure,[79] as shown in S.5 (Supporting Information). The layer thickness was fixed at 50 µm for all prints. The objects were printed with an illumination time of 4.6 s for the first two layers and 1.0 s for the subsequent layers when using the isotropic formulation. For the nematic formulation, the exposure time was reduced to 0.6 s for the initial two layers and 0.1 s for the following ones. For the isotropic LCE formulation, magnetic nanoparticles were aligned by applying a magnetic field of 10 mT for 2 min before polymerization. For the nematic LCE formulation, mesogen alignment was achieved by exposing the resin to a 100 mT magnetic field for 15 min. Following the alignment phase, the printing process was initiated without disturbing the resin. After printing, the samples were rinsed in ethanol to remove uncured resin. Control samples were fabricated in the absence of any magnetic field, under otherwise identical printing conditions, to serve as unaligned references.

Magnetic Device: Details on the device used to introduce magnetic anisotropies into the photocurable formulations were reported in the S.1 (Supporting Information).

UV Postprocessing: After printing, the samples were subjected to UV post-curing using the Asiga Flash curing chamber for 10 min to ensure complete polymerization and enhance the mechanical properties of the material.

Differential Scanning Calorimetry Measurements (DSC): The test were performed using a PerkinElmer DSC 7 system (Shelton, USA) to investigate the thermal transitions of various resin formulations. Approximately 7 mg of each sample was placed in 30 ul aluminum DSC pans from the same manufacturer and sealed. The thermal protocol consisted of an initial isothermal hold at 20 °C for 1 min, followed by heating to 100 °C at a rate of 20 °C min^{-1}. After a 1-min isotherm at 100 °C, the samples were cooled back to 20 °C at the same rate. The melting temperature (T_m) and the nematic–isotropic transition temperature (T_{ni}) were determined from the first heating cycle. T_m was identified as the minimum of the first endothermic peak, corresponding to the phase transition of the mesogens from the crystalline to the nematic state. T_{ni} was determined as the minimum of the second endothermic peak, associated with the phase transition of the mesogens from the nematic to the isotropic state.

Optical Microscopy: Images were acquired using a LEICA DM microscope (Nanterre, France) equipped with a CCD K3C camera and a cross-polarizer to enhance contrast in anisotropic structures. The system was configured with ocular lenses and objective lenses providing magnifications of 10× and 50×. This setup enabled the visualization of microstructural features and alignment patterns within the material using the LAS X software.

Wide-Angle X-Ray Scattering (WAXS): The SAXS–WAXS experiments were performed at the Laboratoire Interdisciplinaire sur l'Organisation Nanométrique et Supramoléculaire (LIONS), CEA–CNRS, Université Paris-Saclay, NIMBE, France. The measurements were carried out using

a commercial Xeuss 3.0 instrument (XENOCS). The beam diameter at the sample position was 0.7 mm, delivering approximately 5×10^7 photons s^{-1}. For the WAXS configuration, the sample was placed at a distance of 0.041 m (normal incidence point) from the detector, providing a q-range from 0.1 to 3.9 $Å^{-1}$. The acquisition time was 300 s. The order parameter (S) was calculated using the following equation[55]

$$S = \frac{\int_0^{\frac{\pi}{2}} I(\theta)\, \frac{3\cos^2\theta - 1}{2} \sin\theta d\theta}{-\frac{1}{2}\int_0^{\frac{\pi}{2}} I(\theta)\, \sin\theta d\theta} \quad (3)$$

where θ is the angle between the director and mesogenic units, and $I(\theta)$ is the azimuthal intensity distribution. The calculation was carried out for θ between 0 and 90°.

Finite Element Simulation of Thermo-Responsive Liquid Crystal Elastomer: To numerically simulate these deformations, the LCE was modelled as an incompressible thermoelastic solid with temperature-dependent thermal expansion behavior. Upon heating, the LCE contracts along its nematic direction, which refers to the magnetically aligned direction set during the DLP printing, and expands slightly in the two other orthogonal directions. This anisotropic deformation was represented by assigning a negative coefficient of thermal expansion (CTE) along the nematic direction and a transversely isotropic expansion (nonuniform) in the perpendicular directions. The contractile thermal strain along the nematic direction was denoted as e_T, while the expansion in the transverse directions was approximated as $-e_T/2$. The thermal strain depends only on the current temperature T and a reference temperature of the material T_{ref}, at which the strain was zero. This LCE model serves as the active material in all case studies presented in this paper. For the Finite element (FE) simulations, both types of layers were meshed using C3D8R elements in the commercial software Abaqus (Version 2023, Dassault Systèmes, Vélizy-Villacoublay, France). A linear elastic material was employed instead of a hyperelastic one due to the limitation of Abaqus in handling anisotropic thermal expansion in hyperelastic formulations. The material behavior was adapted from Peng et al. and from Athinarayanarao et al.[80,81] and calibrated with experimental tests. Specifically, the anisotropic thermal expansion coefficients were derived experimentally from uniaxial thermomechanical tests on magnetically aligned LCE samples. The longitudinal thermal strain (along the nematic direction) was directly measured as a function of temperature. The corresponding transverse expansion was assumed to satisfy volume conservation, resulting in a strain ratio of approximately– 1/2 in the perpendicular directions. These experimentally derived values were used to define the direction-dependent coefficients of thermal expansion in the FE model. In the numerical simulations, a uniform mesogen alignment was assumed, consistent with the magnetostatic simulations shown in Figure S1 (Supporting Information). The observed bending of the bilayer structures arises from the mismatch in the coefficients of thermal expansion between the two layers, a property that was governed by their respective crosslink densities. Figure S19 (Supporting Information) shows the FE predictions corresponding to the printed cases illustrated in Figure 2.

Electrical Characterization: The 3D-printed samples were first contacted by sputter-depositing a 100 nm gold layer on both surfaces using a Quorum Q150T S sputter coater system. Resistivity and current–voltage (I–V) characteristics were measured using a Keithley 4200A-SCS Source Measure Unit in a two-point probe configuration. Tungsten microneedles were used to contact the top and bottom surfaces of the printed samples (5 × 5 mm). Measurements were performed using a linear voltage sweep in the range of ±5 V, with a scan step of 0.1 V and a current compliance limit set at 70 mA. The reported I–V curves represent the average of three measurement cycles.

Morphological Characterization: Samples were prepared in cross-section at room temperature using a Leica UC7 ultramicrotome. Imaging was performed using field emission scanning electron microscopy (FE-SEM) with a Hitachi S-4800, equipped with an EDX system for compositional analysis. All images were acquired in high-vacuum mode at an accelerating voltage of 10 keV.

Supporting Information

Supporting Information is available from the Wiley Online Library or from the author.

Acknowledgements

E.A. and A.C. contributed equally to the work. The authors gratefully acknowledge Sami Laroui (LMS, École Polytechnique) for his assistance with conductive measurements, Florian Aubrit (LSI, École Polytechnique) for providing the FESEM images, and Laurance Bodelot (LMS, École Polytechnique) for support with mechanical testing. EA, GCR, and DL also thank Olivier Tache and Emeline Cournede (CEA-Saclay, NIMBE-LIONS) for their support with WAXS measurements at the SWAXS platform. This work has been funded by the National Research Agency (ANR) through the France 2030 program PEPR DIADEM Artemis (ANR-22-PEXD-0016), and by the Commissariat a l'Energie Atomique et aux Energies Alternatives (CEA) through the project Functional-DLP of the Program Transversal de Competences (PTC). Simulations were made possible through the support of the "Mésocentre" computing center of CentraleSupélec and Ecole Normale Supérieure Paris-Saclay, supported by CNRS and Région Ile-de-France (http://mesocentre.centralesupelec.fr/). This research benefited from the support of the École Polytechnique fundraising initiative, Smart Environments: Nanosensors and Nanoreliability, through the use of the PLATINE platform. The WAXS measurements were made possible thanks to the support of the SWAXS platform, part of the PEPR DIADEM program (ANR-22-PEXD-0001). The magnetic device, designed for integration with additive manufacturing systems to enable magnetically-assisted 3D printing, has been patented under No. WO2025073835A1.[70]

Conflict of Interest

The authors declare no conflict of interest.

Data Availability Statement

The data that support the findings of this study are available in the supplementary material of this article.

Keywords

4D printing, digital light processing, liquid crystal elastomers (LCE), magnetic 3D printing, magnetic actuation, thermal actuation, thermo-magnetic actuation

Received: September 10, 2025
Revised: October 22, 2025
Published online: November 24, 2025

[1] F. Xu, B. L. Feringa, *Adv. Mater.* **2023**, *35*, 2204413.
[2] M. Cheng, Q. Liu, G. Ju, Y. Zhang, L. Jiang, F. Shi, *Adv. Mater.* **2014**, *26*, 306.
[3] P. Cataldi, M. Liu, M. Bissett, I. A. Kinloch, *Adv. Mater. Technol.* **2022**, *7*, 2200025.
[4] S. Ahmadi, Y. Fatahi, M. Safarkhani, M. Rabiee, M. E. Warkiani, N. Rabiee, *ACS Symp. Ser.* **2023**, *1436*, 31.
[5] T. Manouras, M. Vamvakaki, *Polym. Chem.* **2017**, *8*, 74.
[6] G. Filipcsei, I. Csetneki, A. Szilágyi, M. Zrínyi, *Oligomers-Polymer Composites-Molecular Imprinting*, Springer, Berlin, New York **2007**.

[7] A. Cosola, M. Sangermano, D. Terenziani, R. Conti, M. Messori, H. Grützmacher, C. F. Pirri, A. Chiappone, *Appl. Mater. Today* **2021**, *23*, 101060.
[8] A. Cortés, J. L. Aguilar, A. Cosola, X. X. Fernández Sanchez-Romate, A. Jiménez-Suárez, M. Sangermano, M. Campo, S. G. Prolongo, *ACS Appl. Polym. Mater.* **2021**, *3*, 5207.
[9] A. Cortés, A. Cosola, M. Sangermano, M. Campo, S. González Prolongo, C. F. Pirri, A. Jiménez-Suárez, A. Chiappone, *Adv. Funct. Mater.* **2021**, *31*, 2106774.
[10] A. Cosola, I. Roppolo, F. Frascella, L. Napione, G. Barrera, P. Tiberto, F. Turbant, V. Arluison, I. Caldelari, N. Mercier, M. Castellino, F. Aubrit, G. Rizza, *Adv. Funct. Mater.* **2024**, *34*, 2406226.
[11] I. Roppolo, M. Caprioli, C. F. Pirri, S. Magdassi, *Adv. Mater.* **2024**, *36*, 2305537.
[12] M. Gastaldi, I. Roppolo, A. Chiappone, C. Garino, A. Fin, M. Manachino, P. Sirianni, G. Viscardi, L. Scaltrito, M. Zanetti, S. Bordiga, C. Barolo, *Addit. Manuf.* **2022**, *49*, 102504.
[13] S. Lantean, G. Barrera, C. F. Pirri, P. Tiberto, M. Sangermano, I. Roppolo, G. Rizza, *Adv. Mater. Technol.* **2019**, *4*, 1900505.
[14] S. Lantean, I. Roppolo, M. Sangermano, M. Hayoun, H. Dammak, G. Rizza, *Addit. Manuf.* **2021**, *47*, 102343.
[15] S. Lantean, I. Roppolo, M. Sangermano, M. Hayoun, H. Dammak, G. Barrera, P. Tiberto, C. F. Pirri, L. Bodelot, G. Rizza, *Adv. Mater. Technol.* **2022**, *7*, 2200288.
[16] C. Zhang, X. Li, L. Jiang, D. Tang, H. Xu, P. Zhao, J. Fu, Q. Zhou, Y. Chen, *Adv. Funct. Mater.* **2021**, *31*, 2102777.
[17] S. C. Ligon, R. Liska, J. Stampfl, M. Gurr, R. Mülhaupt, *Chem. Rev.* **2017**, *117*, 10212.
[18] J. W. Stansbury, M. J. Idacavage, *Dental Mater.* **2016**, *32*, 54.
[19] I. Gibson, D. Rosen, B. Stucker, M. Khorasani, *Additive Manufacturing Technologies*, 2nd edition, Springer, Princeton, New Jersey **2015**.
[20] V. D. Sagias, K. I. Giannakopoulos, C. Stergiou, *Proc. Struct. Integr.* **2018**, *10*, 85.
[21] A. Tariq, Z. U. Arif, M. Y. Khalid, M. Hossain, P. I. Rasool, R. Umer, S. Ramakrishna, *Adv. Eng. Mater.* **2023**, *25*, 2301074.
[22] F. Demoly, M. L. Dunn, K. L. Wood, H. J. Qi, J.-C. André, *Mater. Des.* **2021**, *212*, 110193.
[23] F. Demoly, J.-C. André, *Between Disruptive Research and Industrial Applications*, John Wiley & Sons, Hoboken, NJ **2022**.
[24] F. Demoly, J. C. André, *Between Science and Technology*, John Wiley & Sons, Hoboken, NJ **2022**.
[25] T. A. Campbell, O. S. Ivanova, *Nano Today* **2013**, *8*, 119.
[26] J. Z. Manapat, Q. Chen, P. Ye, R. C. Advincula, *Macro Materials & Eng.* **2017**, *302*, 1600553.
[27] R. D. Farahani, M. Dubé, D. Therriault, *Adv. Mater.* **2016**, *28*, 5794.
[28] *Additive Manufacturing of Polymer-Based Composite Materials* (Eds: F. Touchard, F. Sarasini), Elsevier, Amsterdam, Netherlands **2024**.
[29] Y. Min, M. Akbulut, K. Kristiansen, Y. Golan, J. Israelachvili, *Nature Mater.* **2008**, *7*, 527.
[30] J. N. Israelachvili, *Intermolecular and Surface Forces*, Academic Press, Cambridge, Massachusetts **2011**.
[31] G. B. Jeffery, *Proc. R. Soc. Lond. A* **1922**, *102*, 161.
[32] T. D. Papathanasiou, D. C. Guell, *Flow-Induced Alignment in Composite Materials*, Woodhead Publishing Limited, Sawston, Cambridge, England **1997**.
[33] A. Sydney Gladman, E. A. Matsumoto, R. G. Nuzzo, L. Mahadevan, J. A. Lewis, *Nature Mater.* **2016**, *15*, 413.
[34] B. Bar-On, X. Sui, K. Livanov, B. Achrai, E. Kalfon-Cohen, E. Wiesel, H. D Wagner, *Appl. Phys. Lett.* **2014**, *105*, 033703.
[35] A. Ozcelik, J. Rufo, F. Guo, Y. Gu, P. Li, J. Lata, T. J. Huang, *Nat. Methods* **2018**, *15*, 1021.
[36] D. E. Yunus, S. Sohrabi, R. He, W. Shi, Y. Liu, *J. Micromech. Microeng.* **2017**, *27*, 045016.
[37] S. Shabaniverki, J. J. Juárez, *Micromachines* **2021**, *12*, 935.
[38] J. Greenhall, F. G Vasquez, B. Raeymaekers, *Appl. Phys. Lett.* **2016**, *108*, 103103.
[39] S. Cai, Y. Sun, Z. Wang, W. Yang, X. Li, H. Yu, *Nanotechnol. Rev.* **2021**, *10*, 1046.
[40] D. Shin, S. Choi, J. Kim, A. Regmi, J. Chang, *Adv. Mater. Technol.* **2020**, *5*, 2000232.
[41] K. Kim, W. Zhu, X. Qu, C. Aaronson, W. R. McCall, S. Chen, D. J. Sirbuly, *ACS Nano* **2014**, *8*, 9799.
[42] T. Gissibl, S. Thiele, A. Herkommer, H. Giessen, *Nature Photon* **2016**, *10*, 554.
[43] W. C. Liu, V. H. Y. Chou, R. P. Behera, H. L. Ferrand, *Nat. Commun.* **2022**, *13*, 5015.
[44] D. Kokkinis, M. Schaffner, A. R. Studart, *Nat. Commun.* **2015**, *6*, 8643.
[45] J. Zhao, L. Zhang, J. Hu, *Adv. Intell. Syst.* **2022**, *4*, 2100065.
[46] K. M. Herbert, H. E. Fowler, J. M. McCracken, K. R. Schlafmann, J. A. Koch, T. J. White, *Nat. Rev. Mater.* **2021**, *7*, 23.
[47] R. S. Kularatne, H. Kim, J. M. Boothby, T. H. Ware, *J. Polym. Sci. B Polym. Phys.* **2017**, *55*, 395.
[48] T. Zang, J. Wang, G. Yan, X. Lu, J. Hu, H. Xia, Y. Zhao, *Adv. Mater.* **2025**, *37*, 08694.
[49] T. Zang, S. Fu, J. Cheng, C. Zhang, X. Lu, J. Hu, H. Xia, Y. Zhao, *Chem. Bio Eng.* **2024**, *1*, 488.
[50] T. Zang, R. Muhetaer, C. Zhang, S. Fu, J. Cheng, X. Lu, J. Hu, H. Xia, Y. Zhao, *Macromol. Rapid Commun.* **2025**, *46*, 2500134.
[51] C. M. Yakacki, M. Saed, D. P. Nair, T. Gong, S. M. Reed, C. N. Bowman, *RSC Adv.* **2015**, *5*, 18997.
[52] G. E. Bauman, J. M. McCracken, T. J. White, *Angew. Chem., Int. Ed.* **2022**, *61*, 202202577.
[53] R. K. Shaha, A. H. Torbati, C. P. Frick, *J. Appl. Poly. Sci.* **2021**, *138*, 50136.
[54] H.-H. Yoon, D.-Y. Kim, K.-U. Jeong, S. Ahn, *Macromolecules* **2018**, *51*, 1141.
[55] R. Mouhoubi, V. Lapinte, S. Blanquer, *Adv. Funct. Mater.* **2025**, *35*, 2424400.
[56] J. A. Herman, R. Telles, C. C. Cook, S. C. Leguizamon, J. A. Lewis, B. Kaehr, T. J. White, D. J. Roach, *Adv. Mater.* **2024**, *36*, 2414209.
[57] Y. Wang, J. An, H. Kim, S. Jeong, H. Kim, J. Park, S. Ko, J. Son, H. Lee, *arXiv preprint* **2024**, arXiv:2401.06590.
[58] M. Tabrizi, T. H. Ware, M. R. Shankar, *ACS Appl. Mater. Interfaces* **2019**, *11*, 28236.
[59] Y. Sun, L. Wang, Z. Zhu, X. Li, H. Sun, Y. Zhao, C. Peng, J. Liu, S. Zhang, M. Li, *Adv. Mater.* **2023**, *35*, 2302824.
[60] E. R. Espíndola-Pérez, J. Campo, C. Sánchez-Somolinos, *ACS Appl. Mater. Interfaces* **2024**, *16*, 2704.
[61] S. Miao, Y. Xing, X. Li, B. Sun, Z. Du, H. Cao, P. Guo, Y. Chang, Y. Tian, M. Yao, K. Chen, D. Xiao, X. Zhang, B. Zhao, K. Pan, J. Sun, X. Liang, *Appl. Mater. Today* **2024**, *40*, 102413.
[62] T. Xu, J. Zhang, M. Salehizadeh, O. Onaizah, E. Diller, *Sci. Rob.* **2019**, *4*, aav4494.
[63] Y. Kim, H. Yuk, R. Zhao, S. A. Chester, X. Zhao, *Nature* **2018**, *558*, 274.
[64] J. J. Martin, B. E. Fiore, R. M. Erb, *Nat. Commun.* **2015**, *6*, 8641.
[65] T. Nakamoto, S. Marukado, *Int. J. Autom. Technol.* **2016**, *10*, 916.
[66] Y. Dai, D. Chen, S. Liang, L. Song, Q. Qi, L. Feng, in *2019 IEEE Int. Conf, on Robotics and Biomimetics (ROBIO)*, IEEE, Dali, China **2019**.
[67] P. Blümler, *Cells* **2021**, *10*, 2708.
[68] J. Mallinson, *IEEE Trans. Magn.* **1973**, *9*, 678.
[69] K. Halbach, *Nucl. Instrum. Methods* **1980**, *169*, 1.
[70] G. Rizza, A. Cosola, *WO2025073835A1*, **2025**.
[71] H. Raich, P. Blümler, *Concepts Magn. Reson.* **2004**, *23B*, 16.
[72] A. Wickenbrock, H. Zheng, G. Chatzidrosos, J. Shaji Rebeirro, T. Schneemann, P. Blümler, *J. Magn. Reson.* **2021**, *322*, 106867.
[73] A. Katariya Jain, R. R. Deshmukh, *Liquid Crystals and Display Technology*, (Eds: M. Sasani Ghamsari, I. Carlescu), BoD–Books on Demand, Norderstedt, Germany **2020**.

[74] N. P. Godman, B. A. Kowalski, A. D. Auguste, H. Koerner, T. J. White, *ACS Macro Lett.* **2017**, *6*, 1290.
[75] S. Schuhladen, F. Preller, R. Rix, S. Petsch, R. Zentel, H. Zappe, *Adv. Mater.* **2014**, *26*, 7247.
[76] A. Snezhko, I. S. Aranson, W.-K. Kwok, *Phys. Rev. Lett.* **2005**, *94*, 108002.
[77] J. Kim, S. E. Chung, S.-E. Choi, H. Lee, J. Kim, S. Kwon, *Nature Mater.* **2011**, *10*, 747.
[78] R. M. Erb, J. J. Martin, R. Soheilian, C. Pan, J. R. Barber, *Adv. Funct. Mater.* **2016**, *26*, 3859.
[79] J.-T. Lin, H.-W. Liu, K.-T. Chen, D.-C. Cheng, *Front. Chem.* **2019**, *7*, 760.
[80] X. Peng, S. Wu, X. Sun, L. Yue, S. M. Montgomery, F. Demoly, K. Zhou, R. R. Zhao, H. J. Qi, *Adv. Mater.* **2022**, *34*, 2204890.
[81] D. Athinarayanarao, R. Prod'hon, D. Chamoret, H. J. Qi, M. Bodaghi, J.-C. André, F. Demoly, *npj Comput. Mater.* **2023**, *9*, 1.